



CHORUS

This is the accepted manuscript made available via CHORUS. The article has been published as:

Coulomb scattering rates of excited states in monolayer electron-doped germanene

Po-Hsin Shih, Chih-Wei Chiu, Jhao-Ying Wu, Thi-Nga Do, and Ming-Fa Lin

Phys. Rev. B **97**, 195302 — Published 3 May 2018

DOI: [10.1103/PhysRevB.97.195302](https://doi.org/10.1103/PhysRevB.97.195302)

Coulomb scattering rates of excited states in monolayer electron-doped germanene

Po-Hsin Shih¹, Chih-Wei Chiu², Jhao-Ying Wu^{3,*}, Thi-Nga Do², Ming-Fa Lin^{4,5,*}

¹Department of Physics, National Cheng Kung University, Tainan, 701 Taiwan

²Department of Physics, National Kaohsiung Normal University, Kaohsiung, 824 Taiwan

³Center of General Studies, National Kaohsiung Marine University, Kaohsiung, 811 Taiwan

⁴Hierarchical Green-Energy Materials Research Center, National Cheng Kung University, Tainan, 701, Taiwan

⁵Quantum Topology Center, National Cheng Kung University, Tainan, 701, Taiwan

Abstract

The excited conduction electrons, conduction holes and valence holes in monolayer electron-doped germanene exhibit the unusual Coulomb decay rates. The deexcitation processes are studied using the screened exchange energy. They might utilize the intraband single-particle excitations (SPEs), the interband SPEs, and the plasmon modes, depending on the quasiparticle states and the Fermi energies. The low-lying valence holes can decay by the undamped acoustic plasmon, so that they present very fast Coulomb deexcitations, the non-monotonous energy dependence, and the anisotropic behavior. However, the low-energy conduction electrons and holes are similar to those in the 2D electron gas. The higher-energy conduction states and the deeper-energy valence ones behave similarly in the available deexcitation channels and the dependence of decay rate on wave vector \mathbf{k} .

I. INTRODUCTION

A lot of two-dimensional (2D) materials have been successfully synthesized since the first discovery of graphene in 2004 using the mechanical exfoliation of Bernal graphite [1]. They are very suitable for exploring the diverse physical, chemical, and material properties. Specifically, the 2D IV-group systems possess the high-symmetry honeycomb lattice and the nano-scaled thickness, in which few-layer graphenes have been verified to exhibit the rich and unique properties, such as the massless/massive fermions [2–5], the quantized Landau levels [6–9], the magneto-optical selection rules [10–13], and the quantum Hall effects [14–17]. Recently, few-layer germanene, silicene and tinene are, respectively, grown on [Pt(111), Au(111) & Al(111)] surfaces [18–21], [Ag(111), Ir(111) & ZrBi₂] surfaces [22–24], and Bi₂Te₃(111) surface [25]. Monolayer germanene and silicene, with a stable $\sqrt{3} \times \sqrt{3}$ geometric structure, have been clearly identified from the STM measurements [20,21]. Such systems possess the buckled structures and the significant spin-orbital couplings (SOCs), leading to the rich and unique essential properties [26,27]. They are expected to present the unusual Coulomb excitations/deexcitations arising from many-particle electron-electron interactions. The Coulomb scattering rates of the excited states in monolayer electron-doped germanene are chosen for a model study in this work, especially for their relations with the single-particle and collective electronic excitations.

For germanene, silicene and graphene, the low-lying electronic structures mainly arise from the outmost p_z orbitals [4, 27]. The Dirac-cone structures, being created by the hexagonal symmetry, might be separated or gapless as a result of the significant/negligible SOCs. From an effective Hamiltonian of the tight-binding model (discussed later in Eq. (1)) [27–30], germanene and silicene are predicted to be narrow-gap semiconductors with band gaps of $E_g \sim 93$ meV and ~ 7.9 meV, respectively, reflecting the strengths of SOCs. Moreover, according to the first-principles calculations indicate that the extra Ge adatoms on monolayer germanene could form the dumbbell reconstruction structures [31], and there exist very complicated energy bands initiated from the distinct high-symmetry points. On

the other hand, graphene has linear valence and conduction bands intersecting at the Dirac point in the absence of SOC. The calculated band structures could be examined from the angle-resolved photoemission spectroscopy (ARPES) measurements, as done for few-layer germanene grown on Au(111) surface [19]. The experimental observations indicate that the multiple Dirac-like energy dispersions might be caused by the folding of germanene's Dirac cones. The high-resolution ARPES measurements also provide the full information on the energy widths of the excited states [19,32,33].

The electron-electron interactions are one of the main-stream topics in condensed-matter systems [34–38], since they are responsible for a lot of physical properties, e.g., the effective Coulomb potential, the impurity screening, the correlation energy, the effective mass, and the mean free path. The Coulomb interactions create the many-particle electronic excitations and thus have strong effects on the energies and lifetimes of quasi-particle states. The previous calculations predict that monolayer electron-doped germanene exhibits the diverse momentum- and frequency-dependent phase diagrams [38]. The rich Coulomb excitations, as shown Figs. 1(a) and 1(b) at $E_F = 0.2$ eV, cover the anisotropic excitation spectra, the intraband single-particle excitations (SPEs), the interband SPEs, the strong acoustic plasmon at small momenta (q 's), the second kind of plasmon (the undamped mode at large q 's by the blue arrow in Fig. 1(a)), and the third kind of plasmon accompanied with the intraband Landau damping (the purple arrow in Fig. 1(b)). They might become the effective deexcitation channels of the excited electrons/holes, depending on the wave vectors, valence/conduction states, and Fermi energies. It is worthy of a systematic investigation on the main features/mechanisms of the Coulomb decay rates, and the significant differences among the emergent 2D materials.

The screened exchange energy characterized by the Matsubara's Green functions is used to calculate the Coulomb scattering rates of the excited states in monolayer electron-doped germanene, in which the deexcitation channels are evaluated from the random-phase

approximation (RPA). The decay processes and their dependence on the wave vector, valence/conduction states, and Fermi energy/doping density are explored in detail. A comparison with monolayer graphene is also made. This work shows that the intraband SPEs, the interband SPEs, and the distinct plasmon modes play critical roles in determining the deexcitation behaviors. The unusual Coulomb decay rates are revealed as the oscillatory energy dependence, the strong anisotropy, the non-equivalent valence and conduction Dirac points, and the similarity with 2D electron gas for the low-energy conduction electrons and holes. The predicted Coulomb decay rates could be directly verified from the high-resolution ARPES measurements on the energy widths of quasiparticle state at low temperatures [19, 32, 33].

This work is organized as the following sections. The zero-field Hamiltonian and the RPA self-energy of monolayer electron-doped germanene are derived and discussed in Sec. II. Section III covers the evaluated Coulomb decay rates, the fundamental mechanisms, the experimental examinations, and the comparisons with graphene. Section IV is concluding remarks, accompanied with the effects due to the electron-hole asymmetry, the measured $\sqrt{3} \times \sqrt{3}$ structure, and the predicted dumbbell reconstruction structures.

II. THE RPA SELF – ENERGY

Monolayer germanene has a buckled hexagonal lattice with the Ge-Ge bond length of $b = 2.32 \text{ \AA}$, as shown in Fig. 2(a). There are two equivalent sublattices of A and B, being separated by a distance of $l = 0.66 \text{ \AA}$ (details in [38]). The low-lying electronic structure is dominated by $4p_z$ orbitals. The Hamiltonian, which is built from the sub-space spanned by the four spin-dependent tight-binding functions, is expressed as

$$H = -t \sum_{\langle i,j \rangle, \alpha} c_{i\alpha}^\dagger c_{j\alpha} + i \frac{\lambda_{so}}{3\sqrt{3}} \sum_{\langle\langle i,j \rangle\rangle, \alpha, \beta} \nu_{ij} c_{i\alpha}^\dagger \sigma_{\alpha\beta}^z c_{j\beta} - i \frac{2}{3} \lambda_R \sum_{\langle\langle i,j \rangle\rangle, \alpha, \beta} \mu_{ij} c_{i\alpha}^\dagger (\vec{\sigma} \times \hat{d}_{ij}) c_{j\beta}. \quad (1)$$

The first term, the summation on all the pairs $\langle i, j \rangle$ of the nearest-neighboring lattice sites, is the kinetic energy with the hopping integral of $t = 0.86 \text{ eV}$ [27]. $c_{i\alpha}^\dagger$ ($c_{j\alpha}$) can

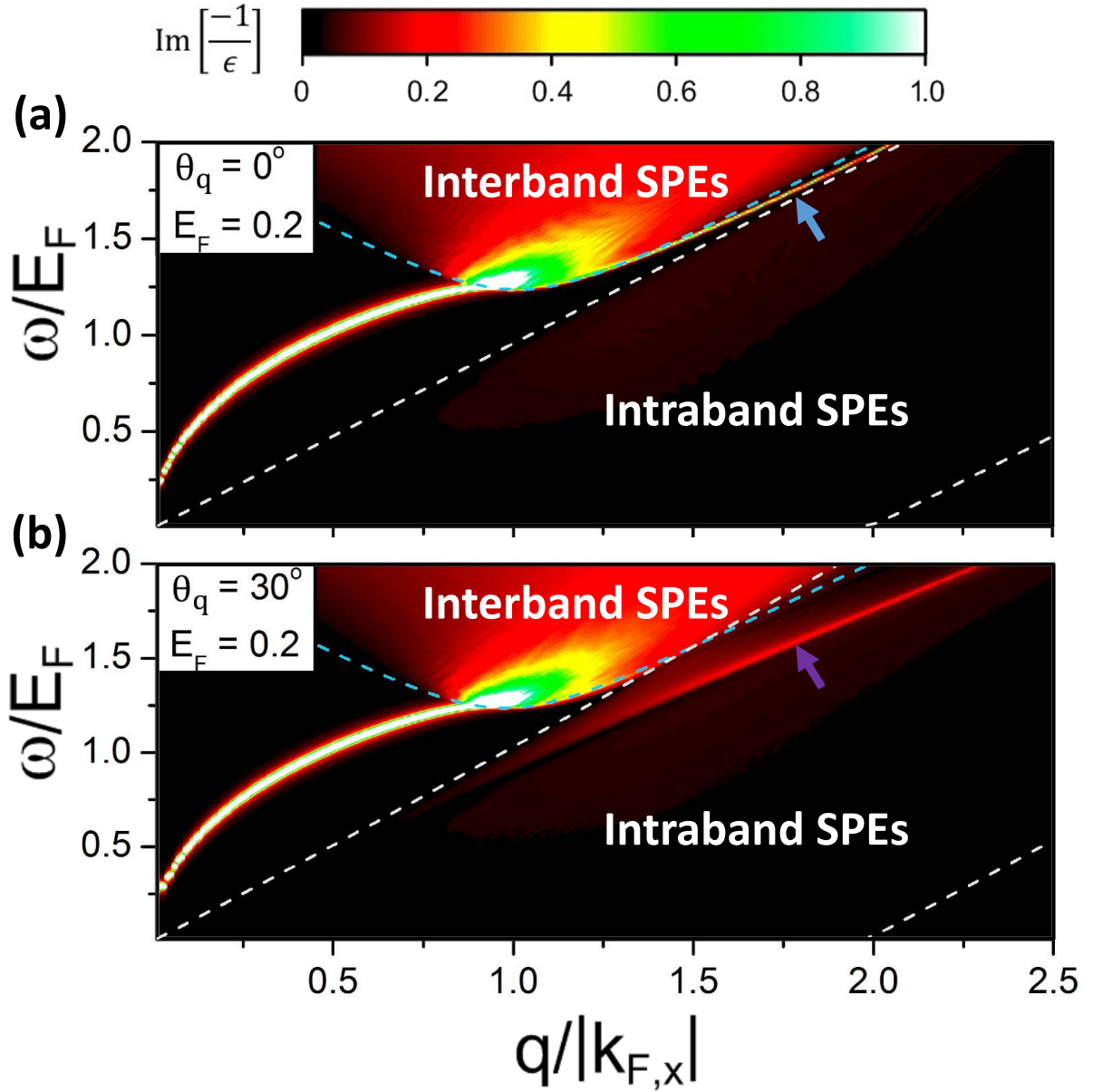


Figure 1: The momentum- and frequency-dependent excitation spectra of germanene with $E_F = 0.2$ eV under (a) $\theta_q = 0^\circ$ and (b) 30° , in which θ_q is the angle between the transferred momentum and ΓM (Fig. 2(b)). The second and third kinds of plasmon modes are, respectively, indicated by the blue and purple arrows in (a) and (b). $k_{F,x}$ is the Fermi momentum along ΓM .

create (annihilate) an electron with spin polarization α (β) at the i -th (j -th) site. The second term represents the effective SOC with the summation on all pairs $\langle\langle i, j \rangle\rangle$ of the next-nearest-neighboring sites, and its strength is $\lambda_{SO} = 46.3$ meV. $\vec{\sigma} = (\sigma_x, \sigma_y, \sigma_z)$ is the Pauli spin matrix. $\nu_{i,j} = (\vec{d}_i \times \vec{d}_j) / |\vec{d}_i \times \vec{d}_j|$, where $\nu_{i,j} = +1$ and -1 , respectively, correspond to the anti-clockwise and clockwise cases from the cross product of the two nearest-neighboring bonding vectors \vec{d}_i and \vec{d}_j . The third term denotes the Rashba SOC with $\lambda_R = 10.7$ meV, $u_{i,j} = +1(-1)$ for the A (B) lattice sites, and \hat{d}_{ij} is the unit vector connecting two sites i and j in the same sublattice (Fig. 2(a)). State energies are characterized by $E^{c,v}(\mathbf{k})$ ($E^h(\mathbf{k})$), where c and v represent conduction and valence states, respectively. They remain doubly degenerate for the spin degree of freedom in the presence of SOC, in which there exists the spin-up- and spin-down-dominated configurations.

The free carrier density and temperature can greatly enrich the electronic excitations of monolayer germanene. Under the perturbation of Coulomb interactions, electrons are excited from the occupied states to the unoccupied ones during the dynamic charge screening. For an intrinsic germanene, only the interband SPEs, being described by the imaginary part of the dielectric function, can survive at zero temperature. The collective excitations are revealed in the loss function as a prominent peak when the free carrier density or temperature is sufficiently high [38]. The extrinsic germanene, with electron doping, is predicted to exhibit three kinds of plasmon modes. There exist intraband and interband SPEs (Figs. 1(a) and 1(b)), in which the former and the latter are, respectively, associated with the conduction and valence carriers. The first kind of plasmon, which behaves as a 2D acoustic mode at small transferred momenta, will make much contribution to Coulomb decay rates. At large q 's, it experiences the heavy interband Landau damping and then disappears. Specifically, the second and third kinds of plasmons come to exist only under the sufficiently large momenta. The above-mentioned single- and many-particle excitation channels are available in the inelastic Coulomb scatterings, as discussed later.

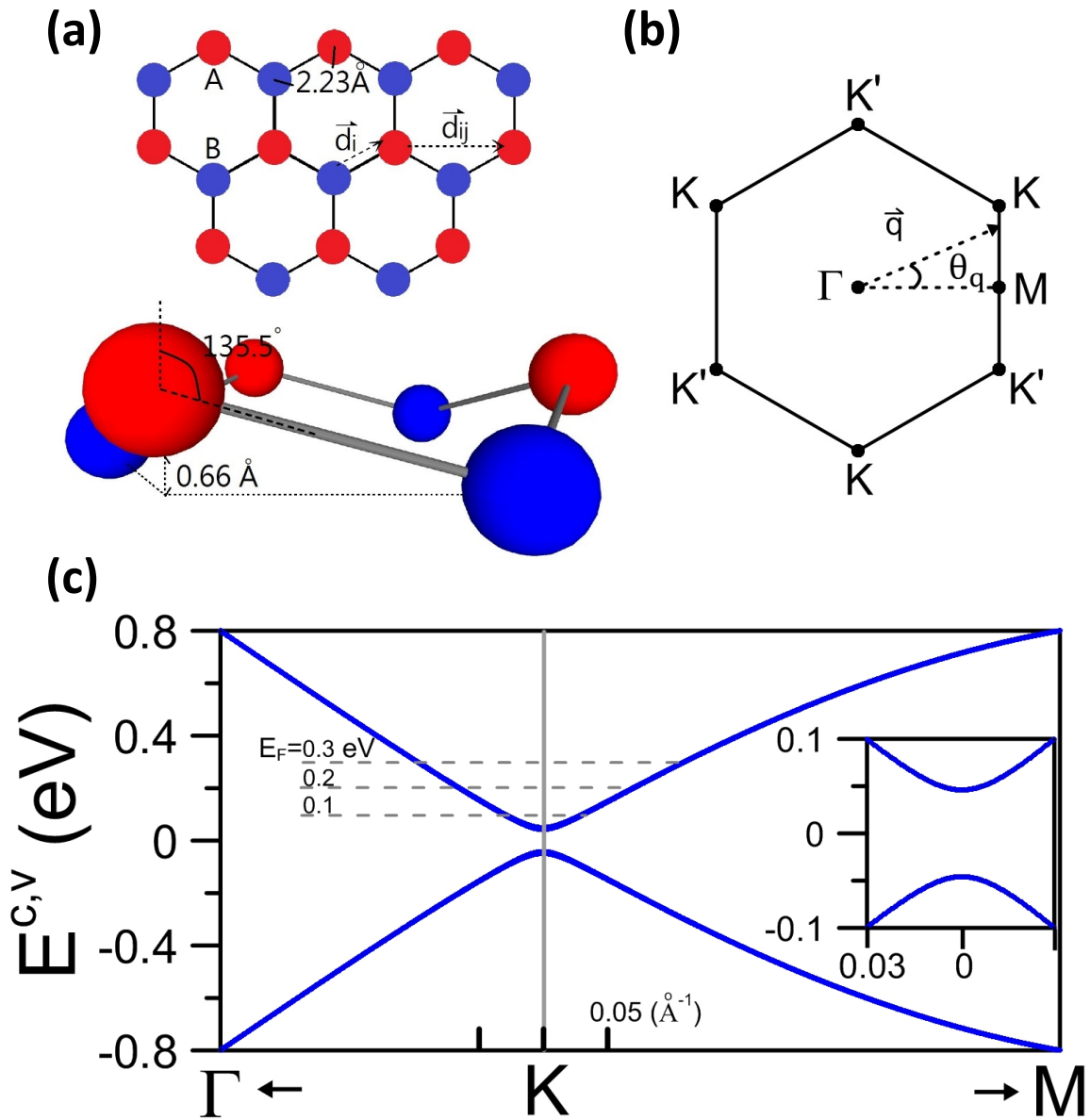


Figure 2: (a) Geometric structure of monolayer germanene shown in the top and side views, (b) the first Brillouin zone, and (c) low-lying energy bands along the high-symmetry points, accompanied with those near the Dirac points in the inset.

The incident electron beam/electromagnetic field has strong interactions with charge carriers and thus creates the excited electrons (holes) above (below) the Fermi level. Such intermediate states could further decay by the inelastic electron-electron scatterings. The Coulomb decay rate ($1/\tau$) is dominated by the effective interaction potential (V^{eff}) between two charges, in which the dynamic e-e interactions could be understood from the RPA. By using the Matsubara Green's functions [39], $1/\tau$ is evaluated from the quasiparticle self-energy, the screened exchange energy

$$\Sigma(\mathbf{k}, h, ik_n) = -\frac{1}{\beta} \sum_{\mathbf{q}, h', i\omega_m} V^{eff}(\mathbf{q}, i\omega_m; \mathbf{k}, h, h') G^{(0)}(\mathbf{k} + \mathbf{q}, h', ik_n + i\omega_m), \quad (2)$$

where $\beta = (k_B T)^{-1}$, $ik_n = i(2n + 1)\pi/\beta$ (complex fermion frequency), $i\omega_m = i2m\pi/\beta$ (complex boson frequency) and $G^{(0)}$ is the noninteracting Matsubara Green's function. $V^{eff}(\mathbf{q}, i\omega_m; h, h', \mathbf{k}) = V_q |\langle h', \mathbf{k} + \mathbf{q} | e^{i\mathbf{q}\cdot\mathbf{r}} | h, \mathbf{k} \rangle|^2 / [\epsilon(\mathbf{q}, i\omega_m)]$ is the screened Coulomb interactions with the band-structure effect, where V_q is the 2D bare Coulomb potential energy and $\epsilon(\mathbf{q}, i\omega_m)$ is the RPA dielectric function. It should be noticed that the SOC leads to the superposition of the spin-up and the spin-down components. However, it does not need to deal with the spin-up- and spin-down-dependent Coulomb decay rates separately, since they make the same contribution. That is, it is sufficient in exploring the wave-vector-, conduction/valence- and energy-dependent self-energy (Eq. (2)). Under the analytic continuation $ik_n \rightarrow E^h(\mathbf{k})$, the self-energy can be divided into the line part and the residue part:

$$\Sigma(\mathbf{k}, h, E^h(\mathbf{k})) = \Sigma^{(line)}(\mathbf{k}, h, E^h(\mathbf{k})) + \Sigma^{(res)}(\mathbf{k}, h, E^h(\mathbf{k})), \quad (3)$$

in which

$$\Sigma^{(line)}(\mathbf{k}, h, E^h(\mathbf{k})) = -\frac{1}{\beta} \sum_{\mathbf{q}, h', i\omega_m} V^{eff}(\mathbf{q}, i\omega_m; \mathbf{k}, h, h') \quad (4)$$

$$\times G^{(0)}(\mathbf{k} + \mathbf{q}, h', E^h(\mathbf{k}) + i\omega_m), \quad (5)$$

and

$$\begin{aligned}
\Sigma^{(res)}(\mathbf{k}, h, E^h(\mathbf{k})) &= -\frac{1}{\beta} \sum_{\mathbf{q}, h', i\omega_m} V^{eff}(\mathbf{q}, i\omega_m; \mathbf{k}, h, h') \\
&\times [G^{(0)}(\mathbf{k} + \mathbf{q}, h', ik_n + i\omega_m) \\
&- G^{(0)}(\mathbf{k} + \mathbf{q}, h', E^h(\mathbf{k}) + i\omega_m)]. \tag{6}
\end{aligned}$$

The imaginary part of the residue self-energy determines the Coulomb decay rate, being defined as

$$\begin{aligned}
\text{Im}\Sigma^{(res)}(\mathbf{k}, h, E^h(\mathbf{k})) &= \frac{-1}{2\tau(\mathbf{k}, h)} \\
&= \sum_{\mathbf{q}, h'} \text{Im}[-V^{eff}(\mathbf{q}, \omega_{de}; \mathbf{k}, h, h')] \\
&\times \{n_B(-\omega_{de})[1 - n_F(E^{h'}(\mathbf{k} + \mathbf{q}))] - n_B(\omega_{de})[n_F(E^{h'}(\mathbf{k} + \mathbf{q}))]\} \\
&= \frac{-1}{2\tau_e(\mathbf{k}, h)} + \frac{-1}{2\tau_h(\mathbf{k}, h)}. \tag{7}
\end{aligned}$$

$\omega_{de} = E^h(\mathbf{k}) - E^{h'}(\mathbf{k} + \mathbf{q})$ is the deexcitation energy. n_B and n_F are the Bose-Einstein and Fermi-Dirac distribution functions, respectively. Equation (7) indicates that an initial state of (\mathbf{k}, h) can be deexcited to all the available $(\mathbf{k} + \mathbf{q}, h')$ states under the Pauli exclusion principle and the conservation of energy and momentum. The excited states above or below the Fermi level are, respectively, related to the electron and hole decay rates (the first and second terms in Eq. (7)). By detailed calculations, the zero-temperature Coulomb decay rates of the excited electrons and holes are

$$\begin{aligned}
\frac{1}{\tau_e(\mathbf{k}, h)} + \frac{1}{\tau_h(\mathbf{k}, h)} &= -2 \sum_{\mathbf{q}, h'} \text{Im}[-V^{eff}(\mathbf{q}, \omega_{de}; \mathbf{k}, h, h')] \\
&\times [-\Theta(\omega_{de})\Theta(E^{h'}(\mathbf{k} + \mathbf{q}) - E_F) + \Theta(-\omega_{de})\Theta(E_F - E^{h'}(\mathbf{k} + \mathbf{q}))]. \tag{8}
\end{aligned}$$

where E_F is the Fermi energy. Θ is the step function that describes the available deexcitation channels. In addition, the decay rate is double the energy width of quasi-particle state.

III. COULOMB DECAY RATES

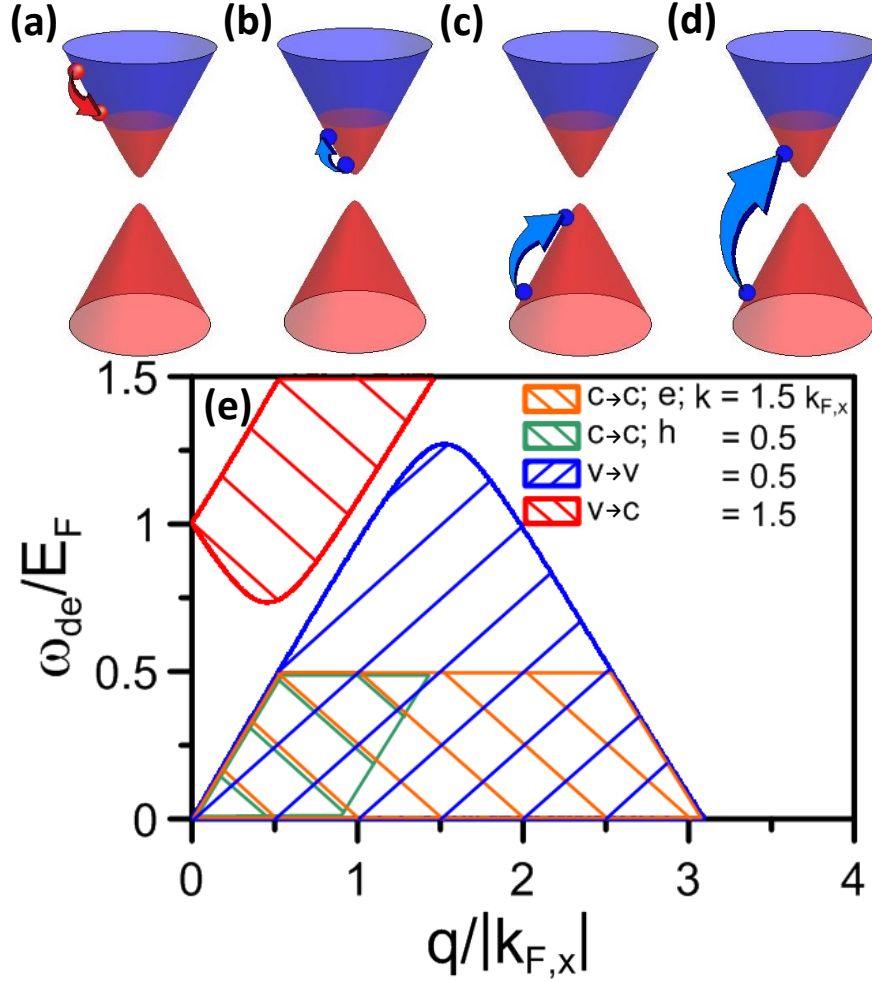


Figure 3: The available deexcitation channels of the specific excited states are indicated for (a) the conduction electrons, (b) the conduction holes, and the valence holes scattered into the (c) same and (d) distinct bands. Furthermore, the relations between the deexcitation energies and transferred momenta are illustrated in (e).

Germanene displays the feature-rich band structure due to the significant SOC and the buckled honeycomb lattice. The conduction band is symmetric to the valence one about the zero energy under an effective Hamiltonian in Eq. (1) (Fig. 2(c)). These two bands present parabolic energy dispersions near the K point (Fig. 2(b)), in which the separated Dirac points have an energy spacing of $E_D = 93$ meV because of SOC (inset in Fig. 2(c)). The state energy, $(E^h(\mathbf{k}))$, is measured from the middle of energy spacing. Energy bands are gradually changed into the linear dispersions in the increase of state energy. Band structure is anisotropic at sufficiently high energies ($|E^{c,v}| > 0.2$ eV), as observed along the $K\Gamma$ and KM directions. With the increasing wave vector, the former exhibits more obvious changes, compared with the latter. The anisotropic energy spectrum will play an important role in the Coulomb scatterings related to the available deexcitation channels.

The Fermi energy/free carrier density dominates the main features of electronic excitations and thus determines the Coulomb decay channels. When E_F is in the middle of energy spacing, the excited electrons/holes at zero temperature can decay into conduction/valence band states only by using the interband SPEs. The increase of E_F creates the intraband SPEs and plasmon modes, and induces the drastic changes in the interband SPEs. Such Coulomb excitations can greatly diversify the decay channels. As for the excited conduction electrons, the final states during the Coulomb deexcitations only lie between the initial states and the Fermi momentum (a red arrow in Fig. 3(a)), according to the Pauli exclusion principle and the conservation of energy and momentum. The available deexcitation channels, the intraband SPEs, make the most important contributions to the Coulomb decay rates for the low-lying conduction electrons, corresponding to the orange part in Fig. 3(e). But when the initial state energy is high, the interband SPEs and the second/third kind of plasmon modes might become the effective deexcitation mechanisms (discussed later in Figs. 5(a) and 4(c)). Concerning the excited holes in the conduction band, they could be de-excited to the conduction states ($c \rightarrow c$; a blue arrow in Fig. 3(b)) through the intraband SPEs, mainly owing to the low deexcitation energies and transferred momenta, as shown

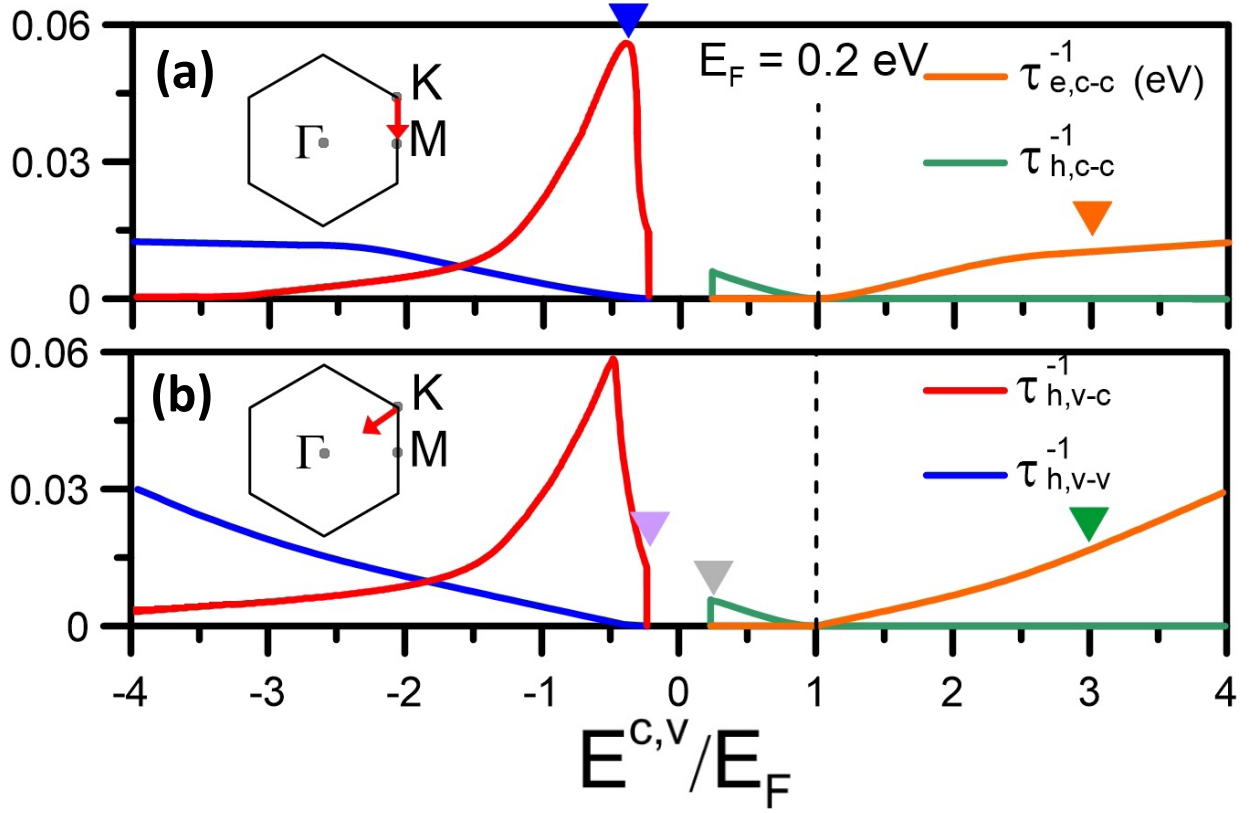


Figure 4: The Coulomb decay rates of the quasi-particle states along the special directions of (a) KM and (b) K Γ are taken into consideration under $E_F = 0.2$ eV.

by the green part in Fig. 3(e). On the other hand, the valence holes present two kinds of decay processes: $v \rightarrow v$ and $v \rightarrow c$ in Figs. 3(c) and 3(d), respectively. Their available decay channels, respectively, cover [intraband SPEs, interband SPEs & the second/third kind of plasmon modes] and [interband SPEs & acoustic plasmon modes], corresponding to the blue and red parts in Fig. 3(e). Specifically, the latter has the large deexcitation energies at small momenta and is thus expected to exhibit the efficient and unusual Coulomb decay rates.

The Coulomb decay rates are very sensitive to the quasiparticle state (\mathbf{k} , h). As to the excited conduction electrons, the $c \rightarrow c$ intraband process is available as state energy gradually increases from the Fermi level. The intraband SPEs make the main contributions to this process (the orange part in Fig. 3(e)); therefore, the decay rate monotonously grows

with E^c , as shown in Figs. 4(a) and 4(b) by the orange curves. When the excited states are close to E_F ($|E^c - E_F| \leq 0.5 E_F$), $1/\tau_e$ is roughly proportional to $(E^c - E_F)^2 \ln|E^c - E_F|$, according to the numerical fitting. Such an energy dependence is characteristic of a 2D electron gas [40, 41]. This is not surprising, since as $E^c \rightarrow E_F$, the deexcitation energy is essential linear in q —whether the energy band has a linear or a quadratic energy dispersion. Furthermore, the low momentum-frequency intraband SPEs are the only deexcitation channels. It is for such reasons that the widths of germanene and electron gas near the Fermi level share a similar character.

For the higher-energy conduction states, the Coulomb decay rates depend on the anisotropic energy bands. Along the KM direction (Fig. 4(a)), $1/\tau_e$ increases and then reaches a saturated value after $E^c > 3E_F$ (an orange arrow). But for the K Γ direction (Fig. 4(b)), it is getting large in the further increase of E^c (a green arrow). This important difference between two directions lies in whether the interband SPEs are the effective deexcitation channels. The higher-energy electronic states have the stronger energy dispersions along K Γ (Fig. 2(c)), so that their deexcitation energies at large transferred momenta are consistent with those of the interband SPEs. For example, the conduction state of $E^c = 3E_F$ along K Γ has a lot of deexcitation channels indicated by the green curve in Fig. 5(a) at $\theta_q = 0^\circ$. The similar results are revealed in the different momentum directions, e.g., the green curves at $\theta_q = 30^\circ$ in Fig. 5(c). The effective deexcitation channels cover the intraband and interband SPEs. The latter is responsible for the enhanced Coulomb decay rates in the high-energy conduction states along K Γ . On the other hand, the $E^c = 3E_F$ conduction electron along KM has the lower deexcitation energies and thus only exhibits the intraband SPEs, as illustrated by the orange curves in Figs. 5(a) and 5(c).

The deexcitation behaviors of the excited holes strongly depend on whether they belong to conduction or valence states. Concerning the conduction holes, the Coulomb decay rates are isotropic, as indicated by the almost identical $\tau_{h,c-c}^{-1}$'s along KM and K Γ (green curves

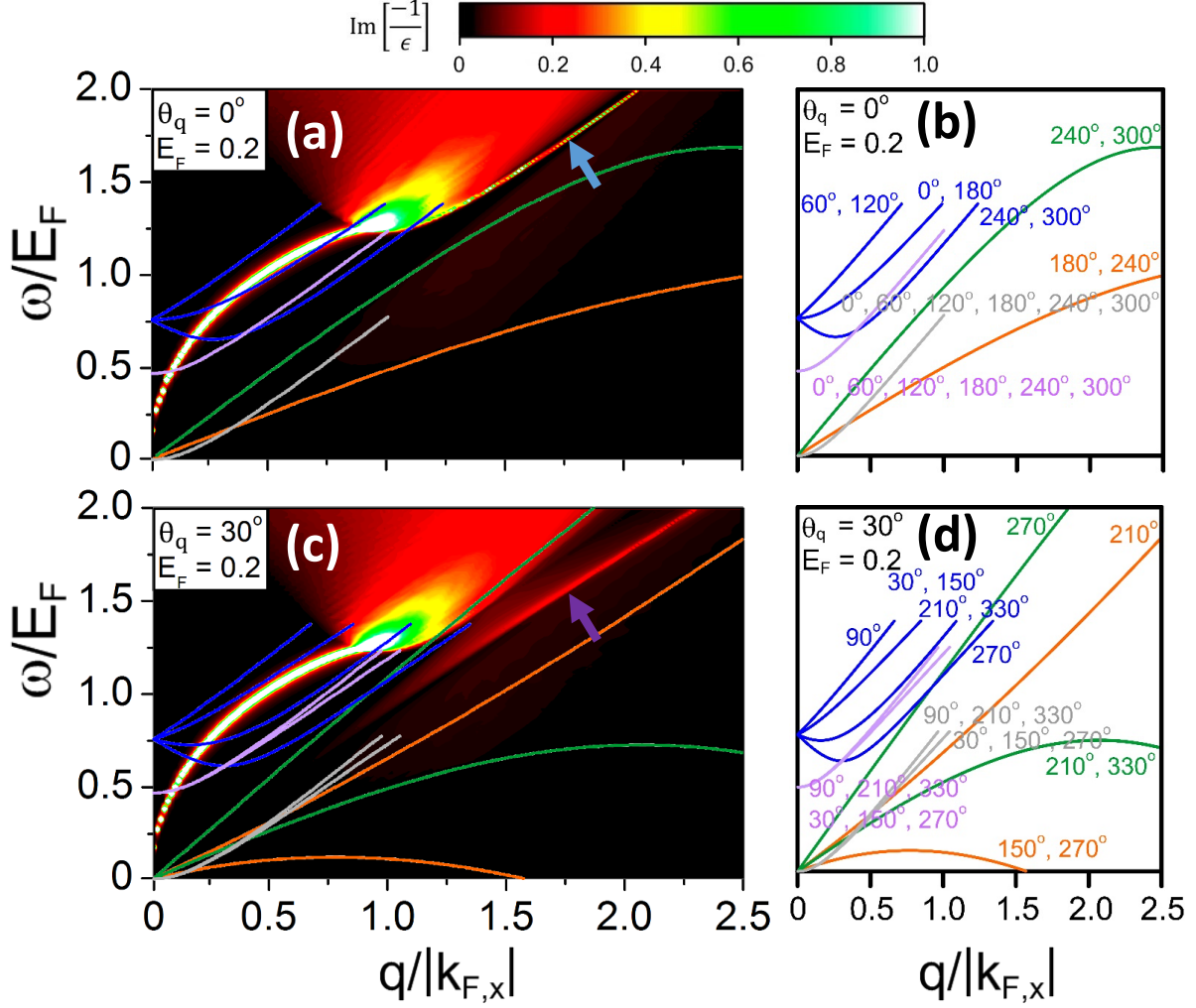


Figure 5: The available deexcitation spectra due to the specific states indicated by the arrows in Figs. 4(a)-4(b) are shown for (a) $\theta_q = 0^\circ$ and (c) $\theta_q = 30^\circ$. The details of the θ_q -dependent deexcitation energies are illustrated in (b) and (d). The curves are defined by the conservation of energy and momentum.

in Figs. 4(a) and 4(b)). Furthermore, the energy dependence is similar to that of the low-lying conduction electrons (2D electron gas). Such results directly reflect the fact that the intraband SPEs are the only available deexcitation channels, e.g., the gray curves related to the conduction Dirac point (Figs. 5(a) and 5(c)). Specifically, the K point (a gray arrow in Fig. 4(b)) has the largest Coulomb decay rate among all the excited conduction holes.

On the other side, the decay rates of the valence holes exhibit the unusual \mathbf{k} -dependences. The valence Dirac point has a significant decay rate (a purple arrow in Fig. 4(b)), being much higher than that of the conduction one. It only presents the $v \rightarrow c$ decay process, in which the deexcitation channels mainly come from the interband SPEs and the undamped plasmon modes, as indicated in the purple curves in Figs. 5(a) and 5(c). They create the important difference between the valence and the conduction Dirac points. With the increase of the valence-state energy, two decay processes, $v \rightarrow c$ and $v \rightarrow v$, contribute to the Coulomb decay rates simultaneously. As to the former, the available range of the strong acoustic plasmon grows and then declines quickly for the low-lying valence holes, leading to an unusual peak structure in $\tau_{h,v-c}^{-1}$ at small E^v 's (the red curve in Figs. 4(a) and 4(b)). For example, the $E^v = -0.4 E_F$ valence state along KM has the widest plasmon-decay range associated with the blue curves in Figs. 5(a) & 5(c), so that it can exhibit the fast Coulomb decay (a blue arrow in Fig. 4(a)). The plasmon-induced deexcitations are almost absent for the deeper valence states (e.g., $E^v < -1.5 E_F$ along KM). The interband SPEs also make some contributions to $\tau_{h,v-c}^{-1}$, and they dominate the Coulomb decay rates of the deeper-energy states, e.g., the red curves along KM and K Γ at $E^v < -2E_F$. Specifically, for the $v \rightarrow v$ process, the excited valence holes (the blue curves in Figs. 4(a) and 4(b) behave as the excited conduction electrons (the orange curves) in terms of the \mathbf{k} -dependence and the deexcitation channels. The intraband SPEs are the dominating mechanisms in determining $\tau_{h,v-v}^{-1}$ of the low-lying valence states ($E^v > -2E_F$). They are replaced by the intraband SPEs and interband SPEs for the deeper valence states along K Γ . This accounts for the anisotropic Coulomb decay rates along K Γ and KM.

The effective deexcitation channels deserve a closer examination. Each excited state could decay along any directions, as clearly indicated by the summation/2D integration of \mathbf{q} in Eq. (7), in which the transferred momentum is a function of q (magnitude) and θ_q (azimuthal angle in the range of 2π). By means of the specific excitation spectrum, it might exhibit several dispersion relations (less than six ones) in the q -dependent deexcitation energies for a fixed θ_q . The main reason is that the Coulomb excitations/energy bands possess the hexagonal symmetry; that is, the excitation spectra are identical for θ_q , $\theta_q + \pi/3$, $\theta_q + 2\pi/3$, $\theta_q + 3\pi/3$, $\theta_q + 4\pi/3$ and $\theta_q + 5\pi/3$. For example, the excited valence hole state, with the highest Coulomb decay rate along KM/K Γ , shows three/four independent dispersive functions (blue curves) for $\theta_q = 0^\circ$ ($\theta_q = 30^\circ$). The other excited states in Figs. 5(a) and 5(c) exhibit the similar behaviors. The total deexcitation regions consist of the θ_q -dependent dispersion relations; that is, they are very sensitive to the direction and magnitude of \mathbf{q} , as expected from the basic scattering pictures. Specifically, Figs. 5(a) and 5(c) clearly show that the excited states along KM and K Γ do not utilize the second and third plasmons as the effective deexcitation channels since the deexcitation energies are insufficient. However, the excited electrons along K Γ , with energies higher than $5E_F$, could decay by the second kind of plasmon mode (not shown). If they are in between KM and K Γ , their energies larger than $3E_F$ will be able to de-excite by the third kind of plasmon mode.

The wave-vector- and Fermi-energy-dependent Coulomb scattering rates, as clearly shown in Figs. 6(a)-6(f), deserve a closer examination. The decay rates of the valence holes exhibit the oscillatory energy dependence along any wave-vector directions, mainly owing to the complicated deexcitation channels. The strongest Coulomb scatterings, being associated with the undamped acoustic plasmons, appear at valence states below the Dirac point (the dashed blue curves in Figs. 6(a), 6(c) and 6(e)). The valence-state decay rates strongly depend on the direction of \mathbf{k} , in which they are, respectively, lowest and highest

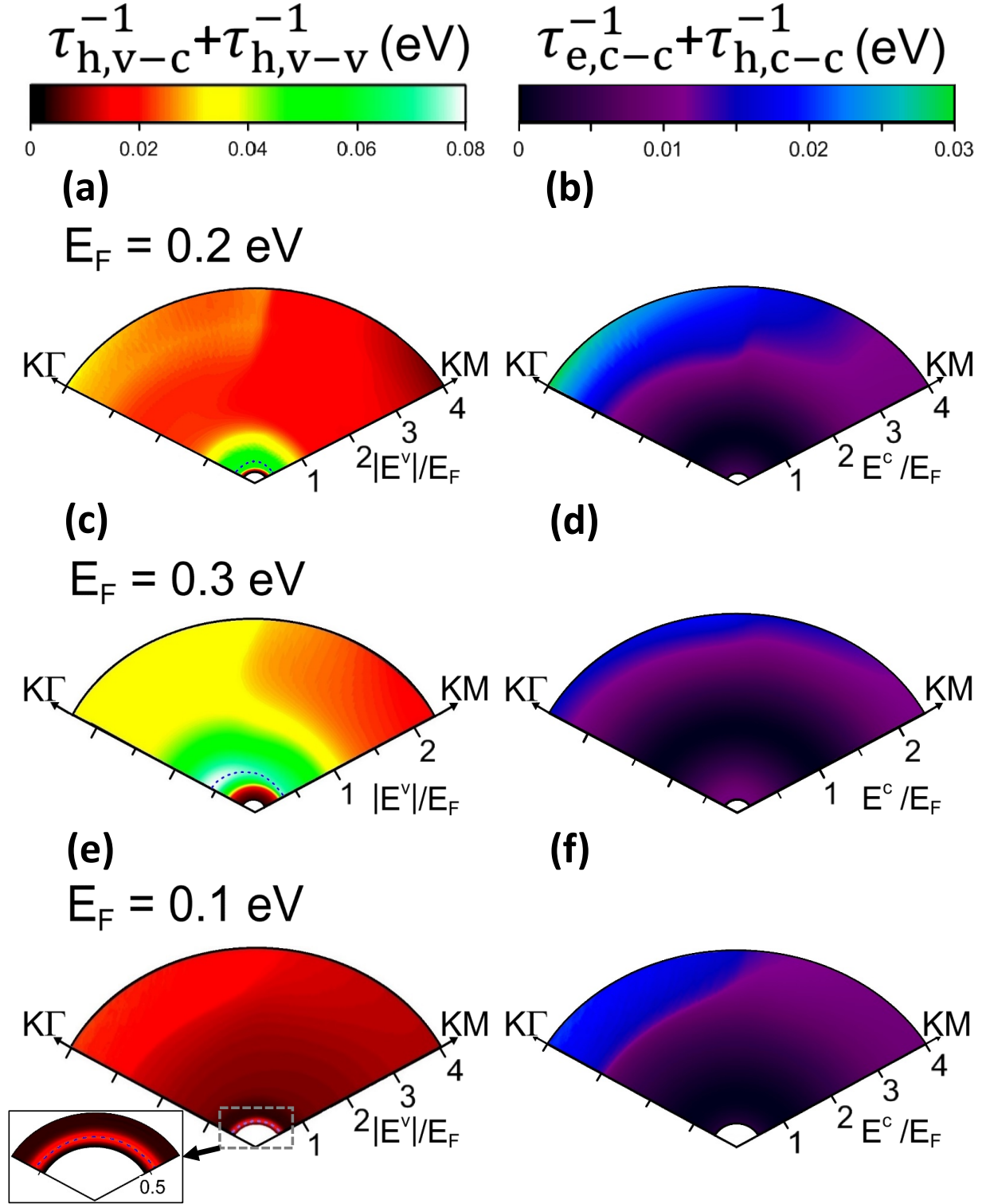


Figure 6: The wave-vector-dependent Coulomb scattering rates of (a) the valence holes and (b) the conduction holes and electrons at $E_F = 0.2$ eV. Similar plots at $E_F = 0.3$ eV and 0.1 eV, are respectively, shown in [(c) & (d)] and [(e) & (f)].

along KM and K Γ . Apparently, there exist the anisotropic Coulomb decay rates for any valence-state energies. This is closely related to the strong anisotropy of the deeper valence band.(Fig. 2(c)). As for conduction holes and electrons, the Coulomb scattering rates, as measured from that of the Fermi-momentum state, present the monotonous energy dependences. The anisotropic deexcitations come to exist only for the higher-energy conduction states.

It is relative to observe the oscillatory energy dependence and the anisotropic behavior at the higher Fermi energy. Electronic excitations and Coulomb decay rates are very sensitive to the changes in free carrier densities, as revealed in Fig. 6. The momentum-frequency excitation spectra are drastically altered by the Fermi energy. For example, the fully undamped intraband plasmon, the almost isotropic excitations, and an obvious excitation gap between the intra- and inter-band SPEs are revealed at the sufficiently low Fermi level, e.g., excitation spectra at $E_F = 0.1$ eV [38]. These are directly reflected in the Coulomb decay rates. For larger E_F , the available momentum-frequency deexcitation range of the strongest acoustic plasmons and the interband SPEs is enhanced, since both of them could coexist together. This leads to the stronger dependence of decay rates on state energy and direction of \mathbf{k} , as clearly indicated from Fig. 6(c) at $E_F = 0.3$ eV and Fig. 6(e) at $E_F = 0.1$ eV. The E_F -induced differences are further illustrated by the Coulomb decay rates of the specific states. For example, the largest decay rates are, respectively, 0.074 eV and 0.081 eV along KM and K Γ at $E_F = 0.3$ eV, while they become 0.022 eV and 0.024 eV at $E_F = 0.1$ eV. Furthermore, the conduction and valence Dirac points present the similar differences in the magnitude of decay rate and the anisotropic behavior.

The effective Hamiltonian in Eq. (1) and the RPA self-energy in Eqs. (2)-(8) are suitable for monolayer germanene, silicene, and graphene, with p_z -dominated band structures. The first system possesses the smallest hopping integral and the largest SOC, so that the essential properties are relatively easily tuned by the external factors, e.g., the carrier dop-

ing, electric field, and magnetic field. Specifically, graphene, with the strongest hopping integral (~ 2.6 eV), exhibits a pair of linearly intersecting valence and conduction at the gapless Dirac points in the absence of SOC, in which the isotropic Dirac-cone structure is further used to investigate the rich and unique physical properties [42–45]. However, there are important differences between germanene and graphene in electronic excitations and Coulomb decay rates. Germanene is predicted to present the anisotropic excitation spectra, the second and third kinds of plasmons, a fully undamped acoustic plasmon under the low doping, and the SOC-dependent excitation boundaries, Such features are absent in graphene [38]. The theoretical calculations have been done for the excited conduction and valence electrons in graphene, indicating the isotropic behavior and a vanishing Coulomb decay rate at the Dirac point [45]. Apparently, the calculated results are different from those in this work.

The predicted scattering decay rates could be examined from the high-resolution ARPES measurements, as successfully done for potassium adsorption on monolayer graphene [33]. The ARPES spectra are measured along KM and K Γ directions for various doping concentrations in monolayer electron-doped graphene, clearly indicating the quasi-particle energy dispersions and the linewidth variations. They are further utilized to get the doping-dependent momentum distribution curves (MDCs). The Lorentzian peak structures are centered at the quasi-particle energies, and they present the full width at half-maximum identified as $-2Im\Sigma^{(res)}$ (the scattering rate). The SPEs and plasmons, as well as the electron-phonon scatterings at finite temperatures, are proposed to explain the unusual energy dependences of MDC linewidths. The ARPES measurements at low temperatures could provide the Coulomb-scattering-dominated MDCs to verify the theoretical predictions. The experimental examinations on monolayer electron-doped germanene are useful in understanding the main features of Coulomb decay rates and the critical deexcitation mechanisms.

IV. CONCLUDING REMARKS

In this work, the Coulomb scattering rates in monolayer electron-doped germanene are investigated using the screened exchange energy, in which the excitation spectra are evaluated within the RPA. The excited states cover the conduction electrons, conduction holes, and valence holes, respectively, creating the decay processes: $c \rightarrow c$, $c \rightarrow c$, and $[v \rightarrow c \text{ \& } v \rightarrow v]$. The low-lying conduction electrons/holes present the isotropic scattering rates, mainly owing to the dominating intraband SPEs. Furthermore, they behave as 2D electron gas in the energy-dependent Coulomb decay rates. The other excited states exhibit the rich and unique \mathbf{k} -dependence, including the oscillatory energy dependence and the strong anisotropy. Specifically, the low-energy valence states have the largest decay rates by means of the undamped acoustic plasmon modes, especially for that along $K\Gamma$. Such deexcitation modes also lead to the important difference between the valence and conduction Dirac points. The deeper valence states and the higher conduction states have the similar deexcitation channels, and so do the \mathbf{k} -dependent decay rates. The intraband SPEs are replaced by the intraband SPEs, the interband SPEs and the second/third kind of plasmon mode during the variation from KM to $K\Gamma$ directions. This is responsible for the anisotropic decay rates. It is relatively easy to observe the unusual Coulomb decay rates at higher Fermi energies. Germanene is different from graphene in excitation spectra and decay rates, being closely related to the strengths of hopping integral and SOC. The theoretical predictions on the energy-band-dominated Coulomb decay rates could be examined from the APRES measurements on the energy widths of quasi-particle states.

As to the symmetric electron-hole band structure (Fig. 2(c)), the momentum- and frequency-dependent excitation spectra are identical for electron and hole dopings, and so do the Coulomb scatterings. That is, the Coulomb decay rates of the excited conduction electrons, conduction holes, and valence holes are, respectively, the same with those of the excited valence holes, valence electrons and conduction electrons under the interchange of electron and hole dopings. On the other hand, the asymmetric valence and conduction

bands about the zero energy might be induced by the partial multi-orbital hybridization (the weak sp^3 bonding), the complicated/interlayer hopping integrals in a buckled system, and the significant interactions with substrate [46, 47]. They might have significant effects on electronic excitations, including the momentum-frequency ranges of intraband and interband SPEs, the diversified plasmon modes (with splitting), the existence of Landau damping (the co-existence of plasmons and SPEs), the spectral anisotropy due to the momentum direction, and the distinct excitation spectra for electron and hole dopings [48]. The available deexcitation channels will become more complicated; therefore, the main features of Coulomb decay rates, the oscillatory energy dependence, and the anisotropic behavior, are expected to be greatly enhanced.

The geometric structures strongly affect the energy bands and thus the electron-electron Coulomb interactions. The measured $\sqrt{3} \times \sqrt{3}$ geometric structure [20, 21] will induce the zone-folding effect on the band structure. More energy subbands and even energy spacings could create complicated excitation spectra and Coulomb scatterings, such as the various intra-band/interband single-particle excitations/deexcitations, and the subband-dominated Coulomb decay rates. Concerning the predicted dumbbell structures [31], the distinct energy bands near the K, Γ and M points arise from the multi-orbital bondings due to the highly buckled structure. Their band structures are quite different from that of the pristine system, and so the other essential properties. The Coulomb excitations and deexcitations will be dramatically changed in terms of the momentum-frequency excitation phase diagrams and the symmetry-point-dependent decay rates.

The RPA is frequently used to study the Coulomb excitations and deexcitations of condensed-matter systems, especially for the high-density carriers in 3D, 2D and 1D materials [34–38, 43–45]. This method might induce the poor results at low free carrier density in certain many-particle properties, mainly owing to the insufficient correlation effects. Some models have been proposed to modify the electron-electron interactions, e.g., the Hubbard

and Singwi-Sjolander models for electronic excitation spectra, and the Ting-Lee-Quinn model for Coulomb decay rates [39]. As to the time-dependent first-principles methods, accompanied with the Bethe-Salpeter equation, are further developed to explore the excitation and deexcitation phenomena in detail [49,50]. Such calculations could account for the experimental measurements on excitation spectra and energy widths under a sufficiently large energy/momentum scale. However, it might be difficult to provide much information about the critical mechanisms/pictures from the numerical calculations. Whether the calculated results are suitable/reliable at low energy is worthy of detailed examinations.

Acknowledgement

This material is based upon work supported by the Air Force Office of Scientific Research under award number FA2386-18-1-0120. We would also like to acknowledge the financial support from the Ministry of Science and Technology of the Republic of China (Taiwan) under Grant No. 105-2112-M-006 -002 -MY3.

References

- [1] K. S. Novoselov, A. K. Geim, S. V. Morozov, D. Jiang, Y. Zhang, S. V. Dubonos, I. V. Grigorieva, and A. A. Firsov, Electric Field Effect in Atomically Thin Carbon Films, *Science* **306**, 5696, 666 (2004).
- [2] K. S. Novoselov, A. K. Geim, S. V. Morozov, D. Jiang, M. I. Katsnelson, I. V. Grigorieva, S. V. Dubonos, and A. A. Firsov, Two-dimensional gas of massless Dirac fermions in graphene, *Nature* **438**, 197 (2004).
- [3] I. Pletikosi, M. Kralj, P. Pervan, R. Brako, J. Coraux, A. T. NDiaye, C. Busse, and T. Michely, Dirac Cones and Minigaps for Graphene on Ir(111), *Phys. Rev. Lett.* **102**, 056808 (2009).
- [4] A. H. Castro Neto, F. Guinea, N. M. R. Peres, K. S. Novoselov, and A. K. Geim, The electronic properties of graphene, *Rev. Mod. Phys.* **81**, 109 (2009).
- [5] P. R. Wallace, The band theory of graphite, *Physical Rev.* **71**, 622 (1947).
- [6] Z. Jiang, E. A. Henriksen, L. C. Tung, Y. J. Wang, M. E. Schwartz, M. Y. Han, P. Kim, and H. L. Stormer, Infrared Spectroscopy of Landau Levels of Graphene, *Phys. Rev. Lett.* **98**, 197403 (2007).
- [7] C. L. Lin, R. Arafune, R. Kawahara, M. Kanno, N. Tsukahara, E. Minamitani, Y. Kim, M. Kawai, and N. Takagi, Substrate-Induced Symmetry Breaking in Silicene, *Phys. Rev. Lett.* **110**, 076801 (2013).
- [8] Y. H. Lai, J. H. Ho, C. P. Chang, and M. F. Lin, Magnetoelectronic properties of bilayer Bernal graphene, *Phys. Rev. B* **77**, 085426 (2008).
- [9] C. Lin, J. Wu, Y. Ou, Y. Chiu, and M. Lin, Magneto-electronic properties of multilayer graphenes, *Phys. Chem. Chem. Phys* **17**, 26008 (2015).

- [10] C. Casiraghi, A. Hartschuh, E. Lidorikis, H. Qian, H. Harutyunyan, T. Gokus, K. S. Novoselov, and A. C. Ferrari, Rayleigh Imaging of Graphene and Graphene Layers, *Nano Lett.* **7**, 9, 2711 (2007).
- [11] Y. Kim, Y. Ma, A. Imambekov, N. G. Kalugin, A. Lombardo, A. C. Ferrari, J. Kono, and D. Smirnov, Magnetophonon resonance in graphite: High-field Raman measurements and electron-phonon coupling contributions, *Phys. Rev. B* **85**, 121403 (2012).
- [12] M. Koshino and T. Ando, Magneto-optical properties of multilayer graphene, *Phys. Rev. B* **77**, 115313 (2008).
- [13] C. Lin, T. Do, Y. Huang, and M. Lin, Optical Properties of Graphene in Magnetic and Electric fields, IOP Book, ISBN 978-0-7503-1566-1.
- [14] Y. B. Zhang, Y. W. Tan, H. L. Stormer, and P. Kim, Experimental observation of the quantum Hall effect and Berry's phase in graphene, *Nature* **438**, 201 (2005).
- [15] C. Chang, J. Zhang, X. Feng, and J. Shen, et al. Experimental Observation of the Quantum Anomalous Hall Effect in a Magnetic Topological Insulator, *Science* **340**, 6129, 167 (2013).
- [16] C. L. Kane and E. J. Mele, Quantum Spin Hall Effect in Graphene, *Phys. Rev. Lett.* **95**, 226801 (2005).
- [17] T. Do, C. Chang, P. Shih, and M. Lin, Stacking-enriched magneto-transport properties of few-layer graphenes, *Phys. Chem. Chem. Phys* **19**, 29525 (2017).
- [18] L. Li, S. Z. Lu, J. Pan, Z. Qin, Y. Wang, Y. Q. Wang, G. Cao, S. Du, and H. Gao, Buckled Germanene Formation on Pt(111), *Adv. Mater.* **26**, 4820 (2014).
- [19] N. B. M. Schrter, M. D. Watson, L. B. Duffy, M. Hoesch, Y. Chen, T. Hesjedal, and T. K. Kim, Emergence of Dirac-like bands in the monolayer limit of epitaxial Ge films on Au(111), *2D Mater.* **4**, 031005 (2017).

- [20] M. E. Davila, L. Xian, S. Cahangirov, A. Rubio, and G. Le Lay, Germanene: a novel two-dimensional germanium allotrope akin to graphene and silicene, *New J. Phys.* **16**, 095002 (2014).
- [21] M. Derivaz, D. Dentel, R. Stephan, M. C. Hanf, A. Mehdaoui, P. Sonnet and C. Pirri, Continuous Germanene Layer on Al(111), *Nano Lett.* **15**, 2510 (2015).
- [22] P. Vogt, P. De Padova, C. Quaresima, J. Avila, E. Frantzeskakis, M. C. Asensio, A. Resta, B. Ealet, and G. Le Lay, Silicene: Compelling Experimental Evidence for Graphenelike Two-Dimensional Silicon, *Phys. Rev. Lett.* **108**, 155501 (2012).
- [23] L. Meng, Y. Wang, L. Zhang, S. Du, R. Wu, L. Li, Y. Zhang, G. Li, H. Zhou, W. A. Hofer, and H. J. Gao, Buckled Silicene Formation on Ir(111), *Nano Lett.* **13**, 685 (2013).
- [24] A. Fleurence, R. Friedlein, T. Ozaki, H. Kawai, Y. Wang and Y. Y. Takamura, Experimental Evidence for Epitaxial Silicene on Diboride Thin Films, *Phys. Rev. Lett.* **108**, 245501 (2012).
- [25] F. Zhu, W. Chen, Y. Xu, C. Gao, D. Guan, C. Liu, D. Qian, S. Zhang, and J. Jia, Epitaxial growth of two-dimensional stanene, *Nature Materials* **14**, 1020 (2015).
- [26] Z. Ni, Q. Liu, K. Tang, J. Zheng, J. Zhou, R. Qin, Z. Gao, D. Yu, and Jing Lu, Tunable Bandgap in Silicene and Germanene, *Nano Lett.* **12**, 113 (2012).
- [27] C. C. Liu, H. Jiang, and Y. Yao, Low-energy effective Hamiltonian involving spin-orbit coupling in silicene and two-dimensional germanium and tin, *Phys. Rev. B* **84**, 195430 (2011).
- [28] M. Ezawa, A topological insulator and helical zero mode in silicene under an inhomogeneous electric field, *New Journal of Physics* **14**, 033003 (2012).

- [29] S. M. Huang, S. T. Lee, and C. Y. Mou, Ferromagnetism and quantum anomalous Hall effect in one-side-saturated buckled honeycomb lattices, *Phys. Rev. B* **89**, 195444 (2014).
- [30] J. Zheng, F. Chi, and Y. Guo, Exchange and electric fields enhanced spin thermoelectric performance of germanene nano-ribbon, *Journal of Physics: Condensed Matter* **27**, 295302 (2015).
- [31] V. Ongun zelik, E. Durgun, and Salim Ciraci, New Phases of Germanene, *J. Phys. Chem. Lett.* **5** , 2694 (2014).
- [32] C. Heske, R. Treusch, F. J. Himpsel, S. Kakar, L. J. Terminello, H. J. Weyer, and E. L. Shirley, Band widening in graphite, *Phys. Rev. B* **59**, 4680 (1999).
- [33] A. Bostwick, T. Ohta, T. Seyller, K. Horn, and E. Rotenberg, Quasiparticle dynamics in graphene, *Nature Physics* **3**, 36 (2007).
- [34] E. H. Hwang and S. Das Sarma, Dielectric function, screening, and plasmons in two-dimensional graphene, *Phys. Rev. B* **75**, 205418 (2007).
- [35] J. H. Ho, C. L. Lu, C. C. Hwang, C. P. Chang, and M. F. Lin, Coulomb excitations in AA- and AB-stacked bilayer graphites, *Phys. Rev. B* **74**, 085406 (2006).
- [36] C. J. Tabert and E. J. Nicol, Dynamical polarization function, plasmons, and screening in silicene and other buckled honeycomb lattices, *Phys. Rev. B* **89**, 195410 (2014).
- [37] H. R. Chang, J. Zhou, H. Zhang, and Y. Yao, Probing the topological phase transition via density oscillations in silicene and germanene, *Phys. Rev. B* **89**, 201411 (2014).
- [38] P. H. Shih, Y. H. Chiu, J. Y. Wu, F. L. Shyu, and M. F. Lin, Coulomb excitations of monolayer germanene, *Scientific Reports* **7**, 40600 (2017).
- [39] G. D. Mahan, *Many-Particle Physics*, Plenum, New York, 3rd ed. (2000).

- [40] A. V. Chaplik, Energy Spectrum and Electron Scattering Processes in Inversion Layers, *Journal of Experimental and Theoretical Physics* **33**, 5, 997 (1971).
- [41] G. F. Giuliani and J. J. Quinn, Lifetime of a quasiparticle in a two-dimensional electron gas, *Phys. Rev. B* **26**, 4421 (1982).
- [42] T. Ando, Screening Effect and Impurity Scattering in Monolayer Graphene, *J. Phys. Soc. Jpn.* **75**, 074716 (2006).
- [43] O. Roslyak, G. Gumbs, and D. Huang, Plasma excitations of dressed Dirac electrons in graphene layers, *Journal of Applied Physics* **109**, 113721 (2011).
- [44] Q. Li and S. Das Sarma, Finite temperature inelastic mean free path and quasiparticle lifetime in graphene, *Phys. Rev. B* **87**, 085406 (2013).
- [45] E. H. Hwang, B. Y. K. Hu, and S. Das Sarma, Inelastic carrier lifetime in graphene, *Phys. Rev. B* **76**, 115434 (2007).
- [46] Z. Ni, E. Minamitani, Y. Ando, and S. Watanabe, Germanene and stanene on two-dimensional substrates: Dirac cone and Z₂ invariant, *Phys. Rev. B* **86**, 075427 (2017).
- [47] Z. Ni, E. Minamitani, Y. Ando, and S. Watanabe, The electronic structure of quasi-free-standing germanene on monolayer MX (M = Ga, In; X = S, Se, Te), *Phys. Chem. Chem. Phys* **17**, 19039 (2015).
- [48] C. W. Chiu, S. H. Lee, S. C. Chen, and M. F. Lin, Electronic excitations in doped monolayer graphenes, *Journal of Applied Physics* **106**, 113711 (2009).
- [49] C. H. Park, F. Giustino, C. D. Spataru, M. L. Cohen, and S. G. Louie, First-Principles Study of Electron Linewidths in Graphene, *Phys. Rev. Lett.* **102**, 189904 (2009).
- [50] L. Hung, F. H. da Jornada, J. Souto-Casares, J. R. Chelikowsky, S. G. Louie, and S. Ogut, Excitation spectra of aromatic molecules within a real-space GW-BSE formalism: Role of self-consistency and vertex corrections, *Phys. Rev. B* **94**, 085125 (2016).